

Experimental and Computational Studies of Low-Temperature M=4 Flow Deceleration by Lorentz Force¹

Munetake Nishihara², John Bruzzese³, Igor V. Adamovich⁴

*Nonequilibrium Thermodynamics Laboratories
Department of Mechanical Engineering
The Ohio State University, Columbus, OH 43201*

Keisuke Udagawa⁵

*Department of Energy Science
Tokyo Institute of Technology
Midori-ku, Yokohama, Kanagawa, 226-8503*

and Datta Gaitonde⁶,

*Computational Sciences Branch
Air Force Research Laboratory
Wright-Patterson AFB, OH 45433*

Abstract

The paper presents results of cold MHD flow deceleration experiments using repetitively pulsed, short pulse duration, high voltage discharge to produce ionization in a M=4 nitrogen flow in the presence of transverse DC electric field and transverse magnetic field. Effective flow conductivity is significantly higher than was previously achieved, $\sigma_{\text{eff}}=0.1$ S/m. MHD effect on the flow is detected from the flow static pressure measurements. Retarding Lorentz force applied to the flow produces a static pressure increase of 19%, while accelerating force of the same magnitude applied to the same flow results in static pressure increase of 11%. The effect is produced for two possible combinations of the magnetic field and transverse current directions producing the same Lorentz force direction (both for accelerating and retarding force). The results of static pressure measurements are compared with predictions of a 3-D Navier-Stokes / MHD flow code. The static pressure rise predicted by the code, 18% for the retarding force and 8% for the accelerating force, agrees well with the experimental measurements. Analysis of the

¹ Copyright ©, American Institute of Aeronautics and Astronautics. All rights reserved

² Post Doctoral Researcher

³ Graduate Research Assistant

⁴ Associate Professor, Associate Fellow AIAA

⁵ Graduate student

⁶ Tech. Area Leader, Associate Fellow AIAA

Report Documentation Page				Form Approved OMB No. 0704-0188	
Public reporting burden for the collection of information is estimated to average 1 hour per response, including the time for reviewing instructions, searching existing data sources, gathering and maintaining the data needed, and completing and reviewing the collection of information. Send comments regarding this burden estimate or any other aspect of this collection of information, including suggestions for reducing this burden, to Washington Headquarters Services, Directorate for Information Operations and Reports, 1215 Jefferson Davis Highway, Suite 1204, Arlington VA 22202-4302. Respondents should be aware that notwithstanding any other provision of law, no person shall be subject to a penalty for failing to comply with a collection of information if it does not display a currently valid OMB control number.					
1. REPORT DATE JUN 2007		2. REPORT TYPE		3. DATES COVERED 00-00-2007 to 00-00-2007	
4. TITLE AND SUBTITLE Experimental and Computational Studies of Low-Temperature M=4 Flow Deceleration by Lorentz Force				5a. CONTRACT NUMBER	
				5b. GRANT NUMBER	
				5c. PROGRAM ELEMENT NUMBER	
6. AUTHOR(S)				5d. PROJECT NUMBER	
				5e. TASK NUMBER	
				5f. WORK UNIT NUMBER	
7. PERFORMING ORGANIZATION NAME(S) AND ADDRESS(ES) Ohio State University, Department of Mechanical Engineering, Columbus, OH, 43210				8. PERFORMING ORGANIZATION REPORT NUMBER	
9. SPONSORING/MONITORING AGENCY NAME(S) AND ADDRESS(ES)				10. SPONSOR/MONITOR'S ACRONYM(S)	
				11. SPONSOR/MONITOR'S REPORT NUMBER(S)	
12. DISTRIBUTION/AVAILABILITY STATEMENT Approved for public release; distribution unlimited					
13. SUPPLEMENTARY NOTES 38th Plasmadynamics and Lasers conference, 25-28 June 2007, Miami, FL					
14. ABSTRACT see report					
15. SUBJECT TERMS					
16. SECURITY CLASSIFICATION OF:			17. LIMITATION OF ABSTRACT Same as Report (SAR)	18. NUMBER OF PAGES 19	19a. NAME OF RESPONSIBLE PERSON
a. REPORT unclassified	b. ABSTRACT unclassified	c. THIS PAGE unclassified			

calculations results shows that at the present conditions, the effects of Joule heating and the accelerating Lorentz force cancel each other, producing nearly zero net flow velocity change. On the other hand, the two effects are combined for the retarding Lorentz force, which results in approximately 2% flow velocity reduction, by $\Delta u=15$ m/sec. This result provides further evidence of cold supersonic flow deceleration by Lorentz force.

1. Introduction

Recent experimental studies of low-temperature MHD flows using ionization produced in the flow by repetitively pulsed nonequilibrium plasmas demonstrated feasibility of MHD high-speed air flow control. In particular, these experiments showed that a retarding Lorentz force results in a density fluctuation increase in a supersonic boundary layer in low-temperature $M=3$ nitrogen and air flows [1]. MHD power extraction was demonstrated in a cold $M=3$ air flow [2]. Finally, low-temperature $M=3$ air flow deceleration by the Lorentz force was detected from the static pressure measurements [3]. In these experiments, ionization in cold supersonic flows (stagnation temperature $T_0=300$ K) was generated by a high voltage, short pulse duration, high pulse repetition rate discharge, and Faraday current was sustained by transverse DC electric field.

The flow deceleration results of Ref. [3] are consistent with 3-D compressible Navier-Stokes MHD modeling calculations [4], which suggest that Lorentz force flow acceleration and deceleration may indeed be detected at the flow conductivities realized at the conditions of experiments [1,3]. Specifically, for a $M=2.6$ nitrogen flow at a stagnation pressure of $P=1/3$ atm, electrical conductivity of $\sigma=0.1$ mho/m, magnetic field of $B_z=1.5$ T, transverse electric field of $E_y=\pm 300$ V/cm, and the MHD section length of $L=5$ cm, these calculations predict Mach number change by up to $\Delta M \approx \pm 0.2$. This Mach number change corresponds to a relative static pressure change of $\Delta P/\approx \pm 0.3$, which would be easily detectable in the experiment. Note that in the modeling calculations of Ref. [4], Joule heating of the flow by the discharge was completely neglected, since it is well known that in nonequilibrium nitrogen and air plasmas, direct Joule heating is significantly reduced because a major fraction of the electric discharge power, up to $\sim 98\%$ [8], goes to vibrational excitation of nitrogen. Indeed, effective Joule heating factor, α (i.e. the discharge energy fraction going into Joule heating of the flow), measured in our previous experiments [3] is rather low, $\alpha \sim 0.1$. However, we believe that this approach is oversimplified, since it is understood that in the actual low-temperature MHD experiments [2], Joule heating, although significantly reduced, still remains an important factor affecting the results.

The main objective of the present work is to study the effect of the Lorentz force on the flow Mach number, determined from static pressure measurements, and to predict this effect using a 3-D compressible Navier-Stokes / MHD flow modeling code. This work follows up our previous experiments [3] in $M=3$ nitrogen and air flows. However, a new design of the supersonic test section used in the present work helps improving the flow quality and reducing the boundary layer thickness in the test section. Also, the present experiments are conducted in a $M=4$ flow, using a higher power plasma pulse generator producing a higher flow conductivity. Finally, the results of present experiments and modeling calculations will be used to determine whether the MHD flow deceleration effect can be detected by a non-intrusive optical diagnostics technique, Molecular Tagging Velocimetry.

2. Experimental

The experiments have been conducted at the supersonic nonequilibrium plasma/MHD blowdown wind tunnel facility described in greater detail in Refs. [1,3]. Briefly, this facility generates stable and diffuse supersonic nonequilibrium plasmas flows at $M=3-4$ in a uniform magnetic field up to $B=2$ T. Figure 1 shows photographs of a supersonic nozzle / MHD test section / diffuser assembly made of transparent acrylic plastic. The assembly consists of an 5.5 cm long converging-diverging nozzle, 9.5 cm long rectangular channel MHD section, and 10 cm long diffuser section. The side walls of the MHD section (same as the nozzle contoured walls) are diverging at 0.5° each to provide boundary layer relief. The channel height and width at the MHD section entrance are 40 mm and 22 mm, respectively. The flow Mach number in the MHD section can be changed between $M=3$ and $M=4$ by replacing the nozzle and diffuser inserts shown in Fig. 1.

The MHD test section schematic is shown in Fig. 2. Two rectangular plate copper DC electrodes 4.5 cm long and 2 cm wide, each placed into a boron nitride electrode holder, are flush mounted in the top and bottom walls of the channel. Two pulsed electrode blocks, with a 5 cm x 3.5 cm x 0.3 cm rectangular plate copper electrode sandwiched between mica ceramic blocks and acrylic plastic plates are flush mounted in the side walls, as shown in Fig. 2. The pulsed electrode edges are rounded to achieve a more uniform electric field distribution between the electrodes. The gaps between the pulsed electrodes, the ceramic blocks, and the acrylic plates are filled with silicon rubber to prevent corona formation near the high-voltage electrode surface. The test section is equipped with a stagnation pressure tap in the nozzle plenum and with two static pressure taps located in the side wall, one 4 cm upstream of the DC electrode and the other is 1 cm downstream of the DC electrode. Static pressure in the test section was monitored using a high accuracy Omega PX811-005GAV pressure transducer, at a sampling rate of 67 Hz. Optical access to the test section is provided by four pairs of rectangular UV grade fused silica windows (Esco Products) placed into the test section walls 1.5 cm upstream and 1.5 cm downstream of the DC electrodes, as shown in Figs. 1,2. This allows optical emission measurements along both horizontal and vertical line-of-sight.

The wind tunnel operates using a 1200 ft³ dump tank pumped down to 35-40 torr by an Allis-Chalmers 1900 cfm rotary vane vacuum pump. Because of the high back pressure, limited by the vacuum pump cutoff, a step angle diffuser was used downstream of the supersonic test section. The diffuser geometry was determined iteratively, by machining the diffuser inserts to increase the diffuser throat height and to reduce the step angles, until the flow Mach number in the test section, calculated from the static to plenum pressure ratio, became close to the design Mach number. This procedure was used for both $M=3$ and $M=4$ diffusers. The resultant ratio of the diffuser height, h_D , to the supersonic test section height, h_T , and the diffuser step angle are $h_D/h_T=0.69$ and $\alpha_d=6^\circ$ for the $M=3$ diffuser, and $h_D/h_T=0.63$ and $\alpha_d=5^\circ$ for the $M=4$ diffuser. At these conditions, plenum pressure and test section static pressure for the $M=3$ nozzle / diffuser are $P_0=250$ torr and $P_{\text{test}}=9$ torr, and those for the $M=4$ nozzle / diffuser are $P_0=600$ torr and $P_{\text{test}}=4.8$ torr. This corresponds to the flow Mach number of $M=2.80$ and $M=3.85$, respectively. The nozzle throat dimensions are 40 mm x 4.8 mm for the $M=3$ nozzle and 40 mm x 1.8 mm for the $M=4$ nozzle, which gives mass flow rates of $\dot{m}=15$ g/sec and $\dot{m}=14$ g/sec, respectively. The

entire nozzle / test section / diffuser assembly is placed between the poles of a GMW water cooled electromagnet. In the present experiments, for the 6.5 cm distance between the 15 cm diameter poles, the magnetic field at maximum current through the magnet coils of 140 A is $B=1.63$ T. A 10 mm diameter circular hole drilled in the center of each magnet pole provides optical access to the test section through the side walls fused silica windows. The magnetic field direction can be switched by changing the magnet power supply polarity. In the present work, two transverse magnetic field directions are referred to “east” and “west”, respectively.

A high voltage, short pulse duration, high repetitive rate pulse generator (FID GmbH, FPG 60-100MC4) is used for the generation of the plasma in the test section. The pulse generator incorporates high voltage step-up circuits triggered by a fast semiconductor switch, Fast Ionization Dynistor (FID) [5]. The pulser generates high voltage, nanosecond duration pulses (peak voltage 8 kV, pulse duration 4 nsec FWHM) at a pulse repetition of up to 100 kHz. The pulser has four high-voltage output channels, two of them positive polarity and the other two negative polarity. In the present work, the pulser is operated in two different modes, two-channel and four-channel. The first mode is using two output channels (one positive and one negative) connected to the pulsed electrodes in the MHD section by two 3 m long, $75\ \Omega$ coaxial transmission cables, so that two opposite polarity pulses (+8 kV and -8 kV) are sent to the load simultaneously, thereby doubling the incident pulse voltage on the electrodes. In the second mode, four output channels are connected to a four $75\ \Omega$ cable assembly, in which the central wire of one positive polarity cable is connected to the shielding of the other positive polarity cable before the load, and the same connection is used for the negative polarity cables. This connection doubles both the positive and the negative voltage pulse amplitude (to +16 kV and -16 kV, respectively), so that the incident pulse voltage on the electrodes is quadrupled. Note that the actual voltage between the electrodes may be higher than 16 kV and 32 kV for the two-channel and four-channel modes, respectively, because of the incident pulse reflection. In the absence of the load (i.e. when the cables are disconnected from the pulsed electrodes and then the entire high-voltage pulse is reflected), the positive-to-negative voltage at the end of the transmission cables is 32 kV and 64 kV, respectively.

Transverse DC current (sustainer current) in the supersonic flow ionized by the repetitively pulsed discharge is sustained by applying a DC field (up to 500 V/cm) to two DC electrodes flush mounted in the top and bottom nozzle walls, perpendicular both to the flow velocity and to the magnetic field direction, as shown in Fig. 2. The transverse DC field is applied using a DEL 2 kV / 3A power supply operated in a voltage stabilized mode, with a $0.5\ \text{k}\Omega$ ballast. Two inductors 1 mH each are placed in the DC circuit in series with both DC electrodes to attenuate high amplitude current pulses propagating into the DC circuit. Current in the DC sustainer circuit is measured using a Tektronix AM503S current probe. The DC current direction (referred to “up” and “down” here) can be changed by switching the power supply polarity.

As discussed in our previous work [3], generation of decelerating and accelerating Lorentz force using two combinations of current and magnetic field vectors for each is essential to isolation of the Lorentz force effect from the Joule heating effect. If the Lorentz force interaction indeed results in significant flow acceleration, the flow static pressure would decrease for both \mathbf{j} and \mathbf{B} vectors configurations producing an accelerating Lorentz force and increase for the other two configurations producing a retarding Lorentz force. On the other hand, if the electric discharge

power at these conditions remains the same, Joule heating would result in a static pressure increase (i.e. Mach number reduction), which would be the same for all four of these cases. In case when both these factors, Lorentz force and Joule heating, generate comparable effects on the flow, the static pressure dependence on the Lorentz force direction should still be apparent.

In the present work, high-voltage pulse voltage is measured by two different methods, using a back current shunt probe [6,7] and a capacitive probe [7-9]. The schematics of the two probes are shown in Figs. 3,4. Both probes are installed 1.3 m from the load in one of a 3 m long transmission cables, to avoid an overlap of an incident pulse generated by the pulser and a pulse reflected from the load. In the current shunt, twelve low inductance, low capacitance 3 Ω resistors (Xicon SMD chip resistors) are placed in the 1 cm gap cut in the cable shielding, along the circumference of the dielectric material separating the center wire and the shielding of the cable. The resistance of the shunt is $R_{shunt}=0.25 \Omega$. When a high voltage pulse, $U_p(t)$, propagates through the transmission cable, current pulses of the same magnitude, $I(t)=U_p(t)/Z_{trans}$, propagate in the opposite directions through the central wire and the shielding. Here $Z_{trans}=75 \Omega$ is the transmission cable impedance. The voltage drop on the shunt is measured using a BNC coaxial cable ($Z_{BNC}=50 \Omega$) connected in series with a $R_{match}=49.8 \Omega$ impedance matching resistor (Xicon SMD chip), connected to a Lecroy Wavepro 7100A, 1GHz bandwidth oscilloscope with a $R_{term}=50 \Omega$ terminator, as shown in Fig. 3. This resistive voltage divider circuit allows avoiding voltage pulse reflections at the terminator and at the shunt. The pulse voltage is calculated as follows,

$$U_p(t) = \frac{Z_{BNC} + R_{match}}{Z_{BNC}} \frac{Z_{trans}}{R_{shunt}} U_{scope}(t), \quad (1)$$

where $U_{scope}(t)$ is a voltage signal on the oscilloscope, i.e. the pulse voltage is attenuated by a factor of 600. The current shunt was calibrated using a 250 V amplitude, 10 nsec rise time rectangular voltage pulse generated by a custom-made calibration pulse generator.

Figure 4 shows a schematic and an equivalent circuit of the capacitive probe, which operates as a capacitive voltage divider circuit. The feed-through capacitor is custom made of a 1.5 mm x 1.5 mm square copper plate (contact surface) soldered to the tip of a copper wire (central wire of a 50 Ω BNC coaxial cable), insulated by a multi-layer piece of Kapton tape 1 cm wide wrapped around it, and covered with a copper tape sleeve soldered to the shield line of the BNC cable, as shown in Fig. 4. The capacitor is placed into a channel made in the dielectric material between the central wire and the shielding of the 75 Ω high-voltage pulse transmission cable, as shown in Fig. 4. The distance from the central wire of the transmission cable to the contact surface is approximately 1 mm. Stray capacitances between the contact surface and the central wire, C_p , and between the contact surface and the shielding, C_c , such as $C_c \ll C_p$, are shown in Fig. 4. The BNC cable, in series with a $R_{match}=49.8 \Omega$ impedance matching resistor, is connected to the oscilloscope through a terminator, $R_{term}=50 \Omega$. When a high voltage pulse propagating along the transmission cable arrives at the location of the contact surface, the stray capacitors charge and then discharge through the terminator. The pulse voltage is determined from the voltage on the capacitor C_c , measured by the oscilloscope, as follows [7],

$$U_p(t) = A \frac{Z_{BNC} + R_{out}}{Z_{BNC}} \left(U_{scope}(t) + \frac{1}{\tau} \int_0^t U_{scope}(t') dt' \right), \quad (2)$$

where

$$\tau = (Z_{BNC} + R_{match})(C_c + C_p) \quad (3)$$

$$A = \frac{C_p + C_c}{C_c}$$

are the RC circuit time constant and the voltage divider circuit coefficient, $\tau=0.26$ ns and $A=100$, determined using the same 250 V, 10 nsec rise time calibration pulse.

Flow temperature downstream of the MHD test section was inferred from the nitrogen second positive band emission spectra taken using a 5 m long optical fiber (BFL22-200, Thorlabs) with collimators at each end, and a Princeton Instruments Optical Multichannel Analyzer (OMA) with a 0.5 m monochromator, 1200 g/mm grating, and an ICCD camera. Field of view of the optical fiber was mapped using a point light source (~ 0.2 mm aperture), which showed the signal collection region to be a cylinder 2-3 mm in diameter and at least 50 mm long, with signal contribution along the line of sight being very nearly constant. Therefore, for a vertical line-of-sight emission measurement, the signal collection region incorporates both the supersonic core flow and the boundary layers downstream of DC electrodes, while for a horizontal line-of-sight measurement, the signal is collected from the supersonic core flow and from the boundary layers downstream of the pulsed electrodes. Rotational temperature of the flow was inferred using a synthetic spectrum [3] with the accurate nitrogen molecular constants, rotational like intensities, and the experimentally measured slit function of the spectrometer.

3. MHD modeling code

In the present work, numerical simulation of the flow in the supersonic nozzle, MHD test section, and the diffuser was done using a 3-D compressible Navier-Stokes / MHD flow code developed by Gaitonde and described in detail in Refs. [10,11]. The governing equations in a non-dimensional form with Lorentz force and energy interaction terms are written as follows,

$$\frac{\partial \rho}{\partial t} + \nabla \cdot (\rho \vec{U}) = 0 \quad (4)$$

$$\frac{\partial \rho \vec{U}}{\partial t} + \nabla \cdot [\rho \vec{U} \vec{U} + p \vec{I}] - \frac{1}{\text{Re}} \nabla \cdot \vec{\tau} = Q (\vec{j} \times \vec{B}) \quad (5)$$

$$\frac{\partial \rho e}{\partial t} + \nabla \cdot \left[(\rho e + p) \vec{U} - \frac{1}{\text{Re}} (\vec{U} \cdot \vec{\tau}) - \frac{1}{(\gamma - 1) \text{Pr} M^2 \text{Re}} Q_{ht} \right] = \alpha Q (\vec{E} \cdot \vec{j}) \quad (6)$$

$$e = \frac{p}{(\gamma - 1)\rho} + \frac{\vec{U}^2}{2}, \quad (7)$$

where t is the time, ρ is the density, \vec{U} is the velocity vector, p is the pressure, \vec{B} and \vec{E} are the magnetic and the electric fields, respectively, Q_{ht} is the heat conduction term, \vec{I} and $\vec{\tau}$ are identity and shear stress tensors, respectively, and α is the effective Joule heating factor (the discharge energy fraction going into Joule heating of the flow) [3]. The non-dimensional parameters are the Reynolds number, Re , the Prandtl number, Pr , the Mach number, M , and the interaction parameter $Q = \sigma_{\text{ref}} B_{\text{ref}}^2 L_{\text{ref}}^2 / (\rho_{\text{ref}} U_{\text{ref}})$, where σ_{ref} is the electrical conductivity and L_{ref} is the reference length (nozzle throat height). The rest of the reference parameters are parameters in the nozzle throat. Capabilities of the code include full coupling of Navier-Stokes equations with Maxwell's equations [11] and the use of generalized Ohm's law with tensor electrical conductivity incorporating the ion-slip parameter for the low magnetic Reynolds number approximation. However, in the present work transverse magnetic field and transverse electric field, as well as the flow conductivity in the crossed discharge in the MHD section are assumed to be uniform, and the Hall effect is neglected. Transverse electric field was estimated from the DC voltage and the effective flow conductivity, σ_{eff} , was determined from the current voltage characteristic of the DC discharge (see Section 4), so that transverse current was calculated simply as $\vec{j} = \sigma_{\text{eff}} \vec{E}$.

The computational domain extends from the nozzle throat, where the flow is assumed to be uniform at $M=1$, to the end of the diffuser section, where zero axial gradient boundary conditions are imposed. The wall boundary conditions are no-slip, zero pressure gradient, and constant wall temperature ($T=300$ K) conditions. The number of mesh points in the flow direction (x), magnetic field direction (y), and electric field direction (z) is 151, 61, and 51, respectively. Initial conditions are obtained from a quasi-one-dimensional isentropic expansion flow based on the area ratio. The system of Eqs. (4-7) is solved using a first order Beam-Warming method with fourth order Roe-averaged fluxes, until steady state is reached. Further discussion of time-marching strategy and spatial discretization can be found in Ref. [10] and references therein.

4. Results and Discussion

Figure 5 shows a photograph and a schematic of an oblique shock system in the $M=4$ diffuser section visualized by the high voltage repetitively pulsed discharge generated in the MHD section. In the present experiments, the pulser-sustainer discharge appears diffuse and volume filling. However, somewhat brighter emission is observed near the side walls (top and bottom walls in the photograph), i.e. close to the pulsed electrodes, and in the center of the test section. Note that the oblique shocks do not extend through the boundary layer to the test section walls. A linear extrapolation of the shock fronts suggests that the oblique shocks originate somewhat upstream of the 5.5° diffuser step angles, possibly due to flow separation at the compression

corners. The oblique shock wave angle determined from the photograph is approximately $\beta=19^\circ$, which corresponds to the flow Mach number at the end of the test section of $M=3.85$. This is consistent with the static pressure measurements downstream of the MHD section, $P=4.8$ torr for the stagnation pressure of $P_0=600$ torr, which also corresponds to $M=3.85$.

Figure 6 shows incident and reflected high voltage pulses for a single pulse generated during the two-channel pulser operation at atmospheric pressure in the test section, measured by the capacitive probe and by the current shunt. At these conditions, there is no breakdown in the test section, so that the entire pulse is reflected. Incident pulse peak voltages (at $t=30$ nsec) measured by the capacitive probe and by the current shunt are 8.1 kV and 8.3 kV, respectively, while reflected pulse peak voltages (at 50 nsec) are 7.0 kV and 8.0 kV, respectively. Although the peak incident pulse voltage measured by the capacitive probe is somewhat lower than that measured by the current shunt, both measurements resulted in almost the same FWHM of 4.2 ns, rise time of 1.6 ns, and fall time of 1.8 ns. Estimated pulse energy coupled to the load at these conditions, calculated as the difference of the incident and the reflected pulse energies [7,12],

$$W = \int_0^\tau \frac{U_{inc}(t)^2}{Z_{trans}} dt - \int_0^\tau \frac{U_{ref}(t)^2}{Z_{trans}} dt \quad (8)$$

is 0.5 mJ / channel from the capacitive probe signal and 0.3 mJ / channel from the current shunt probe signal. In Eq. (8), $Z_{trans}=75 \Omega$ is the transmission cable impedance. Both numbers are close to each other and are much lower than the incident pulse energy, 3.1 mJ. Note that this result provides an estimate of the uncertainty in the coupled pulse energy measurement. The capacitive probe bandwidth, estimated using the same method as in Ref. [7], is ~ 20 GHz, above which the inductance of the feed-through capacitor may affect the signal. On the other hand, transition frequency of chip resistors used in the current shunt is significantly lower, of the order of 1 GHz, above which their reactivity starts affecting the signal. Also, the reflected pulse measured by the current shunt at the conditions when plasma was generated between the electrodes was very noisy. Because of this, we used the capacitive probe for further incident and reflected pulse energy measurements.

Figure 7 shows incident and reflected pulses measured by the capacitive probe in a two-channel pulsed discharge at pulse repetition rate of $\nu=100$ kHz, for the 1st pulse and for the 4000th pulse (i.e. 40 ms later). These measurements are taken in a $M=4$ nitrogen flow at $P_0=600$ torr, $P_{test}=4.8$ torr, and $B=1.63$ T. It can be seen that the incident pulse peak voltage is 8.1 kV for the 1st pulse and 7.0 kV for the 4000th pulse, while the reflected pulse voltage also decreases. The pulse voltage decrease may be due to residual charge accumulation in the transmission cable and on the pulsed electrodes. Pulse energy coupled to the plasma, calculated from the waveforms of Fig. 7, is 1.1 mJ / channel for the 1st pulse and 0.6 mJ / channel for the 4000th pulse. This corresponds to 60 W / channel time averaged discharge power at $\nu=100$ kHz at the steady state conditions (i.e. 240 W for the four channel operation). However, note that since the coupled pulse energies are rather low and comparable with the coupled pulse energy measured in the absence of the plasma (0.5 mJ / channel), this result has a large uncertainty and could be significantly lower. Basically, these measurements suggest even when a plasma is sustained between the pulsed electrodes, most of the incident pulse energy (at least 80%) is reflected. For comparison, in our previous coupled pulse energy measurements in a $M=3$ nitrogen flow at $B=1.5$ T [3] using the

CPT pulse generator (peak voltage 13-15 kV, pulse duration 30 ns, pulse repetition rate $\nu=40$ kHz), coupled pulse energy was about 1 mJ and the time averaged discharge power was approximately 40 W.

Figure 8 shows oscillograms of DC sustainer current in a $M=4$ nitrogen flow at $P_0=600$ torr, $P_{\text{test}}=4.8$ torr, and $B=1.63$ T, ionized by a $\nu=100$ kHz four-channel pulsed discharge. In Fig. 8, DC power supply voltage is $U_{\text{PS}}=\pm 1.4$ kV and a ballast resistance is $R=0.5$ k Ω . It can be seen that the sustainer current peaks at $I=1.2$ A approximately 3 μs after each ionizing pulse, and decays to $I=0.75$ A before the next pulse. For both DC voltage polarities, the time-averaged sustainer currents are very close, $\langle I \rangle=0.94$ A and 0.93 A, respectively. This corresponds to the time-averaged voltage between the electrodes, $\langle U \rangle = U_{\text{PS}} - \langle I \rangle R = 0.93$ kV and the DC discharge power of 0.87 kW. For comparison, in our previous measurements in $M=3$ nitrogen and air flows [3], ionized by a CPT pulser at $\nu=40$ kHz, the DC discharge current, voltage and power were $\langle I \rangle=0.9$ A, $\langle U \rangle=1.6$ kV, and 1.4 kW, respectively. It can be seen that flow ionization by the FID pulser operated in the four-channel mode produces comparable sustainer currents at significantly lower DC voltages, i.e. the FID pulser generates higher flow conductivity.

This effect is further illustrated by comparing current-voltage characteristics of the sustainer discharge for the two-channel and four-channel operation modes of the FID pulser ($\nu=100$ kHz) in a $M=4$ nitrogen flows, and for the CPT pulser in a $M=3$ nitrogen flow ionized by the CPT pulser ($\nu=40$ kHz) [3], both measured in magnetic field of $B=1.5$ T (see Fig. 9). The effective electrical conductivities for these two cases were determined from linear fits to the current-voltage characteristics, as shown in Fig. 9, $\sigma_{\text{eff}}=0.04$ S/m for the $M=3$ flow / CPT pulser, and $\sigma_{\text{eff}}=0.1$ S/m for the $M=4$ flow / four-channel FID pulser. We conclude that the flow conductivity generated by the FID pulser is indeed significantly higher, by about a factor of 2.5. Note that the scalar flow conductivity, i.e. the conductivity at $B=0$, is somewhat higher, since in the presence of magnetic field the conductivity is reduced due to the Hall effect.

Figure 10 shows plasma emission spectra, $1 \rightarrow 4$ band of nitrogen second positive system ($C^3\Pi_u \rightarrow B^3\Pi_g$), averaged along the horizontal line-of-sight by the optical fiber, taken in the repetitively pulsed discharge with and without DC voltage applied. The flow conditions in Fig. 10 are nitrogen at $P_0=600$ torr, $P_{\text{test}}=4.8$ torr, $B=1.5$ T, with a four-channel pulsed discharge operating at $\nu=100$ kHz. The DC power supply voltage was $U_{\text{PS}}=1.3$ kV. It can be seen that the two spectra are very close to each other, suggesting that flow temperature increase due to the DC discharge is small. As discussed in our previous work [3], at the reduced electric field in the sustainer discharge, $E/N=(3-4) \cdot 10^{-16}$ V $\cdot\text{cm}^2$ (based on the isentropic core flow temperature), most of the discharge energy, up to 90%, goes to vibrational excitation of nitrogen and remains “locked” there due to its slow vibrational relaxation. Figure 11 compares the experimental spectrum without DC voltage applied with two synthetic spectra, one for the $M=3.85$ isentropic core flow temperature of $T=77$ K, and the other is the horizontal line-of-sight averaged spectrum for the temperature distribution predicted by the 3-D Navier-Stokes code with the Lorentz force and Joule heat turned off (see Fig. 12). One can see that the two synthetic spectra are very close, demonstrating that the contribution of warm boundary layers into the line-of-sight spectrum is insignificant. On the other hand, both synthetic spectra somewhat underpredict the flow temperature, since the tail of the experimental spectrum is higher than that of the synthetic spectra.

Figure 13 shows normalized test section static pressure traces measured in a $M=4$ nitrogen flow at the plenum pressure of $P_0=600$ torr, with and without Lorentz force applied at the magnetic field of $B=1.63$ T. As in our previous work [3], static pressure was measured for both accelerating and decelerating Lorentz force directions, each generated by two different combinations of transverse B field and transverse current directions. This was done to isolate the polarity-dependent Lorentz force effect from the polarity-independent Joule heat effect. Turning the pulser on in the presence of magnetic field, without applying transverse DC electric field, i.e. generating ionization in the test section without applying Lorentz force resulted in a static pressure increase by 2-3% from the baseline pressure of 4.8 torr, due to Joule heating generated by the pulser (see Fig. 13). The other four pressure traces plotted in Fig. 13 correspond to four different combinations of transverse current vector and magnetic field vector directions, east/up, west/down (both producing accelerating force), west/up, and east/down (both producing retarding force).

As in our previous measurements, the static pressure increased for all four combinations. However, the pressure rise for both accelerating force configurations was higher than for both retarding force configurations (see Fig. 13). Normalized static pressure rise for the retarding and for the accelerating Lorentz force was $\Delta P_R/P=1.19\pm0.03$ and $\Delta P_A/P=1.11\pm0.03$, for the same time-averaged DC currents of $\langle I \rangle=0.93-0.94$ A, as shown in Fig. 9. The normalized baseline pressure (with no Lorentz force applied) was 1.00 ± 0.03 . This effect is consistent with our previous results [3] obtained in $M=3$ nitrogen and air flows ionized by the CPT pulse generator. Basically, static pressure increases due to Joule heating, which is nearly identical in all four cases (see Fig. 8). However, flow acceleration by the Lorentz force reduces the pressure rise, while flow deceleration increases it. Note, however, that in spite of the higher flow conductivity achieved in the present work (a factor of 2.5 higher than in $M=3$ flows, see Fig. 9), the Lorentz force effect on the static pressure is somewhat lower than in our previous work [3]. From the results of Fig. 13, the effective Joule heating factor (i.e. the discharge energy fraction going into Joule heating of the flow) [3],

$$\alpha \cong \frac{\Delta P_A + \Delta P_R}{2} \frac{M^2 - 1}{(\gamma - 1)M} \frac{a}{j_y E_y L} \quad (9)$$

is $\alpha \approx 0.2$. In Eq. (9), $j_y=0.093$ A/cm² is transverse current density, $E_y=230$ V/cm is transverse electric field, $L=4.5$ cm is the length of the MHD section, $M=3.85$, $\gamma=1.4$, and $a=297$ m/s is the speed of sound at $T=77$ K. At the present experimental conditions, the effective loading parameter, i.e. the ratio of Joule heating to the Lorentz force work is $K=\alpha E_y / MaB \approx 4.2$, is nearly the same as in our previous work in $M=3$ flows, $K \approx 4$.

To verify whether the static pressure change shown in Fig. 13 is indeed caused by the flow acceleration and deceleration by the Lorentz force, we used the 3-D Navier-Stokes / MHD flow code briefly described in Section 3. In the calculations, experimental values of flow conductivity, $\sigma_{\text{eff}}=0.1$ S/m, transverse electric field, $E=200$ V/cm, magnetic field, $B=1.5$ T, and effective Joule heating factor, $\alpha=0.2$, were used as entries in the code. Figure 14 shows a contour plot of the Mach number distribution in the $M=4$ nozzle / test section / diffuser for the baseline conditions, $P_0=600$ torr and without plasmas and magnetic field. It can be seen that the Mach number in the

test section peaks at $M=3.85$, which is consistent with the number inferred from the static pressure measurements. Two flow separation regions formed upstream of the diffuser angle steps, weak compression waves in the test section, and oblique shocks in the diffuser are also visible in Fig. 13.

Figure 15 shows axial flow velocity distribution across the flow cross section at the end of the discharge section, for both accelerating and decelerating Lorentz force directions. In this figure, boundary layer bulges formed on the plane walls due to the secondary cross flow are clearly visible. This effect was detected experimentally in our previous work [3], as well as in previous 3-D flow modeling calculations [4]. Although at the present conditions the difference between the accelerated and decelerated flow fields is small, one can see that decelerating force results in the increase of flow separation bubbles inside the boundary layer bulges, as well as in thicker boundary layers on the contoured walls (see Fig. 15).

Figure 16 shows static pressure along one of the plane walls, predicted by the code for baseline, accelerated, and decelerated flows, as well as experimental results such as shown in Fig. 13. One can see that the code somewhat overpredicts the static pressure in the test section (by 10-20%). However, static pressure rise downstream of the MHD section, predicted by the code, is consistent with the experimental measurements. In particular, the predicted pressure rise in the flow decelerated by the Lorentz force is greater than the pressure rise in the accelerated flow, by approximately the same amount. Normalized static pressure rise for the retarding and for the accelerating Lorentz force, predicted by the code, is $\Delta P_R/P=1.18$ and $\Delta P_A/P=1.08$. This result provides further evidence that the static pressure change detected in the present experiments, as well as in our previous work [3], is indeed due to MHD effect.

Figure 17 plots axial velocity for the same three cases as shown in Fig. 16. It can be seen that for the accelerating Lorentz force direction, combination of Joule heating (which decelerates a supersonic flow) and accelerating body force cancel each other and result in a near zero net velocity change. On the other hand, these two effects are combined for the retarding Lorentz force direction, resulting in a velocity reduction by approximately $\Delta u=15$ m/sec at the end of the MHD section (about 2% velocity reduction). Although the predicted flow deceleration is small, we believe that it can be detected by using Molecular Tagging Velocimetry (MTV) optical diagnostics. In this technique, the flow is seeded with a small amount of NO, and the excited electronic state of nitric oxide, $NO(A^2\Sigma)$, is populated by resonance absorption of a pump laser beam at 226 nm. Fluorescence of $NO(A^2\Sigma)$ back to the ground electronic state is monitored after a 0.2-0.6 μ sec delay after the laser pulse. Previous MTV experiments [13] suggests that the uncertainty in the $M=2$ flow velocity measurements using this technique can be only about ~ 1 -2 m/sec. Therefore the MHD flow deceleration effect may well be detected using this diagnostics. These experiments are currently underway.

5. Summary

The paper presents results of cold MHD flow deceleration experiments using repetitively pulsed, short pulse duration, high voltage discharge to produce ionization in a $M=4$ nitrogen flow in the presence of transverse DC electric field and transverse magnetic field. Effective flow

conductivity is significantly higher than was previously achieved, $\sigma_{\text{eff}}=0.1$ S/m. MHD effect on the flow is detected from the flow static pressure measurements. Retarding Lorentz force applied to the flow produces a static pressure increase of 19%, while accelerating force of the same magnitude applied to the same flow results in static pressure increase of 11%. The effect is produced for two possible combinations of the magnetic field and transverse current directions producing the same Lorentz force direction (both for accelerating and retarding force). The results of static pressure measurements are compared with predictions of a 3-D Navier-Stokes / MHD flow code. The fraction of the discharge input power going into Joule heat has been inferred from the present experiments, and used as one of the input parameters in the MHD flow model. The static pressure rise predicted by the code, 18% for the retarding force and 8% for the accelerating force, agrees well with the experimental measurements. Analysis of the calculations results shows that at the present conditions, the effects of Joule heating and the accelerating Lorentz force cancel each other, producing nearly zero net flow velocity change. On the other hand, the two effects are combined for the retarding Lorentz force, which results in approximately 2% flow velocity reduction, by $\Delta u=15$ m/sec. This result provides further evidence of cold supersonic flow deceleration by Lorentz force. The present results suggest that this effect can be detected by Molecular Tagging Velocimetry (MTV) optical diagnostics, which has an uncertainty of about 1-2 m/sec.

6. Acknowledgments

This work has been supported by AFOSR grant FA9550-05-1-0085. The authors would like to thank Dr. Andrei Starikovskii, Dr. Svetlana Starikovskaya (Moscow Institute of Physics and Technology), Dr. Patrick Roblin (Electrical and Computer Engineering Department, The Ohio State University), and Sergey Gorbato (A.V. Lykov Heat and Mass Transfer Institute, Minsk, Belarus) for helpful suggestions on nanosecond pulse energy measurement.

References

1. M. Nishihara, N. Jiang, J.W. Rich, W.R. Lempert, I.V. Adamovich, and S. Gogineni, "Low-temperature supersonic boundary layer control using repetitively pulsed magnetohydrodynamic forcing," *Physics of Fluids*, Vol. 17, 2005, pp. 106102-106102-12
2. R.C. Murray, S.H. Zaidi, M.R. Carraro, L.M. Vasilyak, S.O. Macheret, M.N. Shneider, and R.B. Miles, "Magnetohydrodynamic Power Generation Using Externally Ionized, Cold, Supersonic Air as Working Fluid", *AIAA Journal*, vol. 44, No. 1, 2006, pp. 119-127
3. M. Nishihara, J.W. Rich, W.R. Lempert, I.V. Adamovich, and S. Gogineni, "Low-temperature $M=3$ flow decelerations by Lorentz force," *Physics of Fluids*, Vol. 18, 2006, pp. 086101-086101-11.
4. P. Rawat, X. Zhong, V. Singh, and S. Gogineni, "Numerical Simulation of Secondary Flow in a Weakly Ionized Supersonic Flow with Applied Electromagnetic Field", *AIAA Paper 2005-5050*, 36th AIAA Plasmadynamics and Lasers Conference, Toronto, Ontario, June 6-9, 2005.

5. I.V. Grekhov, S.C.V. Korotkov, A.L. Stepaniants, D.V. Khristyuk, V.B. Voronkov, and Y.V. Aristov, "High-power semiconductor-based nano and subnanosecond pulse generator with a low delay time," *IEEE Transactions on Plasma Science*, Vol. 33, 2005, pp. 1240-1244.
6. L.M. Vasilyak, S.V. Kostyuchenko, A.V. Krasnochub, N.N. Kudryavtsev, and G.A. Kurkin, "An experimental investigation of the electrodynamic and spectral characteristics of a nanosecond pulse-periodic discharge in chlorine," *High Temperature*, Vol. 33, 1995, pp. 822-828.
7. N. Anikin, *Experimental Investigation of Electrodynamical Characteristics of the Fast Ionization Wave in Molecular Gases*, Ph.D. dissertation, Moscow Institute of Physics and Technology, 2000 (in Russian).
8. M.M. Brady and K.G. Dedrick, "High-voltage pulse measurement with a precision capacitive voltage divider," *The Review of Scientific Instruments*, Vol. 33, 1962, pp. 1421-1428.
9. W.R. Fowkes and R.M. Rowe, "Refinements in precision kilovolt pulse measurements," *IEEE Transactions on Instrumentation and Measurement*, Vol. 15, 1966, pp. 284-292.
10. D.V. Gaitonde, "A high-order implicit procedure for the 3-D electric field in complex magnetogasdynamic simulations," *Computers & Fluids*, Vol. 33, 2004, pp. 345-374.
11. D.V. Gaitonde, "High-order solution procedure for three-dimensional nonideal magnetogasdynamics," *AIAA Journal*, Vol. 39, 2001, pp. 2111-2120.
12. É.I. Asinovskii, L.M. Vasilyak, A.V. Kirillin, and V.V. Markovets, "Nanosecond discharge in a weakly ionized plasma," *High Temperature*, Vol. 13, 1975, pp. 32-35.
13. W.R. Lempert, M. Boehm, N. Jiang, S. Gimelshein, and D. Levin, "Comparison of molecular tagging velocimetry data and direct simulation Monte Carlo simulations in supersonic micro jet flow," *Experiments in Fluids*, Vol. 34, 2003, pp. 403-411.

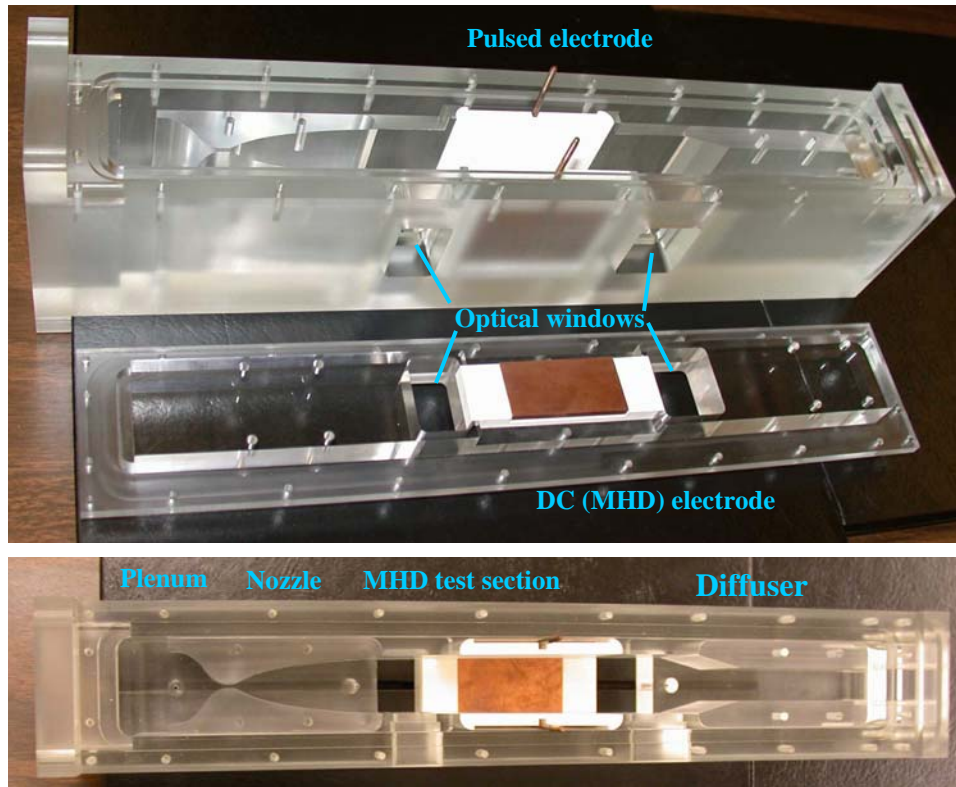


Figure 1. New $M=3$ / $M=4$ supersonic nozzle / MHD test section / diffuser assembly, shown with $M=4$ nozzle inserts in place. Flow is from left to right.

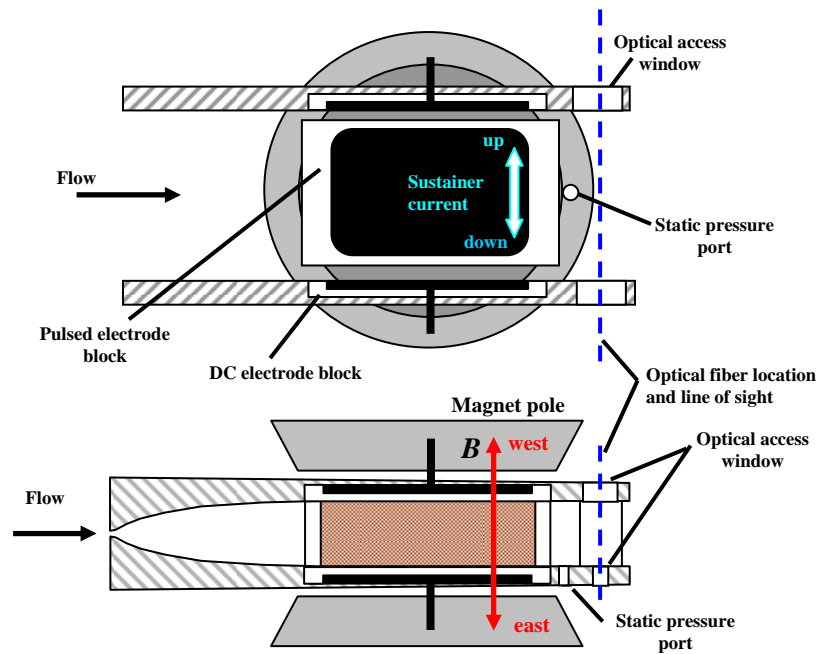


Figure 2. Schematic of a supersonic nozzle and MHD test section.

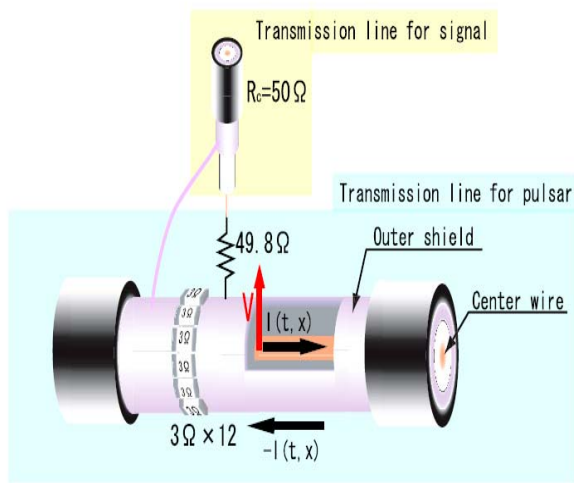


Figure 3. Schematic of a back current shunt.

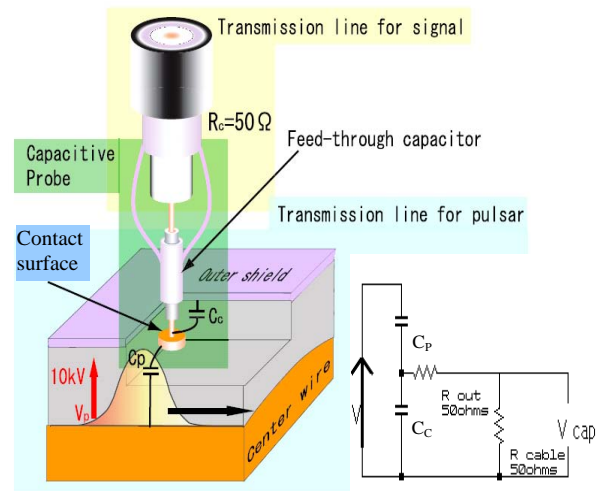


Figure 4. Schematic and an equivalent circuit of a capacitive probe.

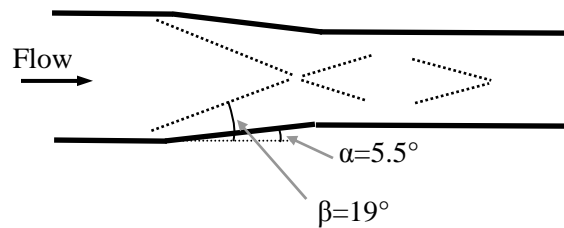
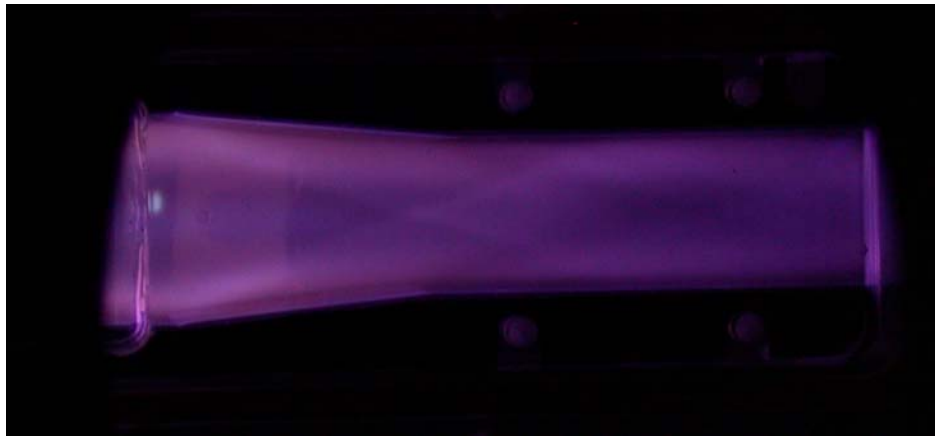


Figure 5. Photograph and schematic of an oblique shock pattern in the $M=4$ diffuser. Nitrogen, $P_0=600$ torr, $P_{\text{test}}=4.8$ torr ($M=3.85$).

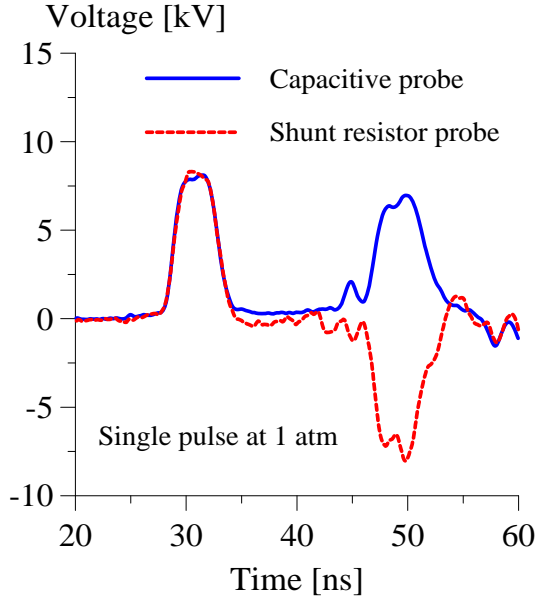


Figure 6. Incident and reflected voltage pulses measured by the capacitive probe and by the back current shunt at the atmospheric pressure in the test section.

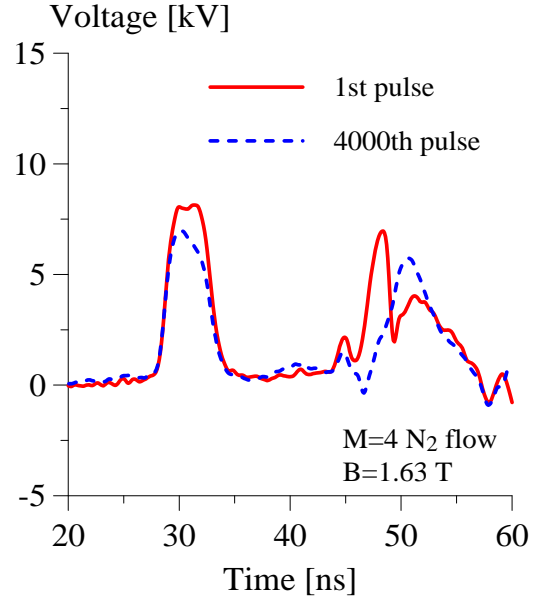


Figure 7. Incident and reflected voltage pulses measured by the capacitive probe for the 1st pulse and for the 4000th pulse. M=4 nitrogen flow, $P_{\text{test}}=4.8$ torr, $B=1.63$ T, $\nu=100$ kHz.

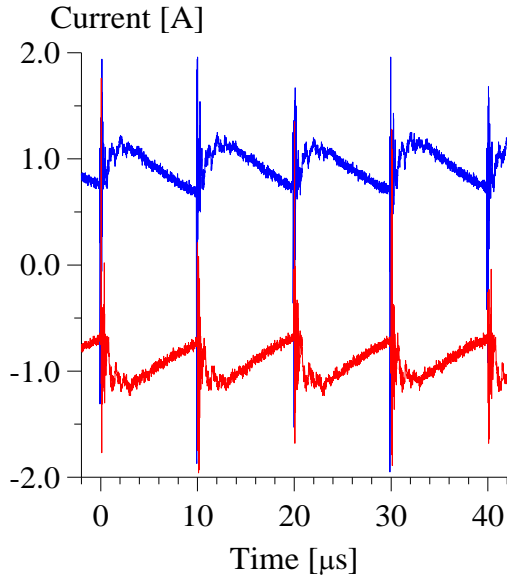


Figure 8. Sustainer current traces for two different transverse DC electric field polarities. M=4 nitrogen flow, $P_0=600$ torr, $P_{\text{test}}=4.8$ torr, $B=1.5$ T, $\nu=100$ kHz, $U_{\text{PS}}=1.4$ kV, $R=0.5$ k Ω . Time-averaged currents are 0.94 A (top curve) and 0.93 A (bottom curve).

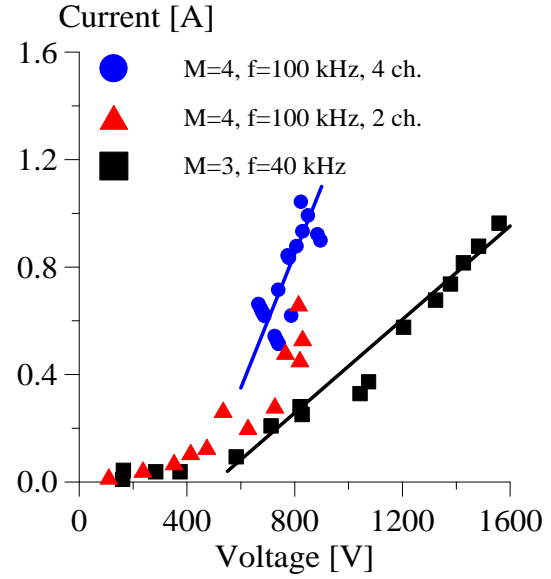


Figure 9. Current voltage characteristics in nitrogen flows at $B=1.5$ T, for different Mach numbers and different pulser operation modes. For M=3, $P_0=250$ torr, $P_{\text{test}}=7.5$ torr, $\nu=40$ kHz. For M=4, $P_0=600$ torr, $P_{\text{test}}=4.8$ torr, $\nu=100$ kHz.

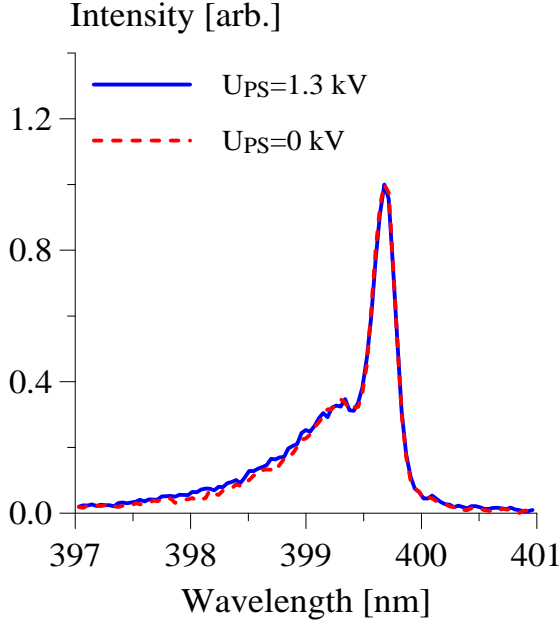


Figure 10. $N_2(C^3\Pi_u \rightarrow B^3\Pi_g)$ emission spectra (1 \rightarrow 4 band) measured along a horizontal line-of-sight in a M=4 nitrogen flow at $P_0=600$ torr, $B=1.5$ T, and $\nu=100$ kHz, with and without 0.9 kW DC sustainer discharge.

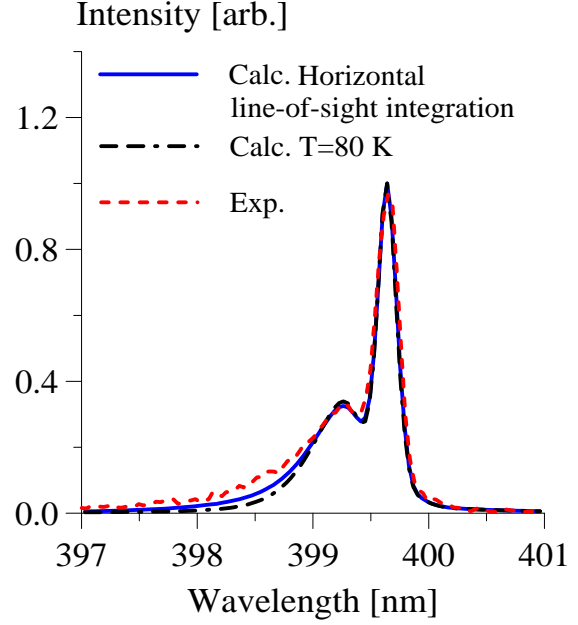


Figure 11. Comparison of experimental spectrum of Fig. 10 (without DC discharge) and synthetic spectra for $T=80$ K and for the temperature distribution predicted by the code for the horizontal line-of-sight (see Fig. 12)

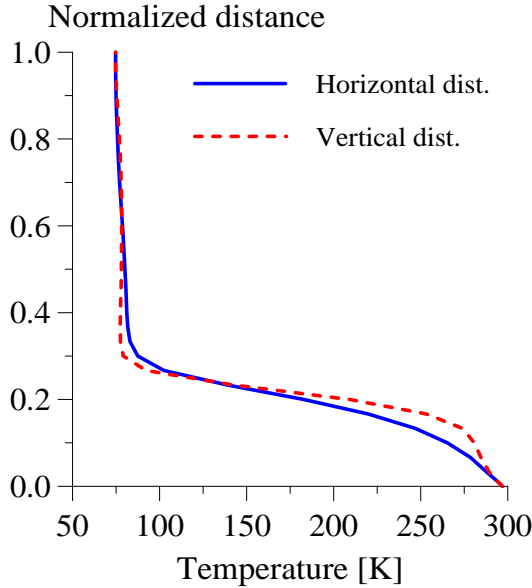


Figure 12. Static temperature distributions along the horizontal and vertical centerlines in a cold M=4 flow (without Joule heating or Lorentz force).

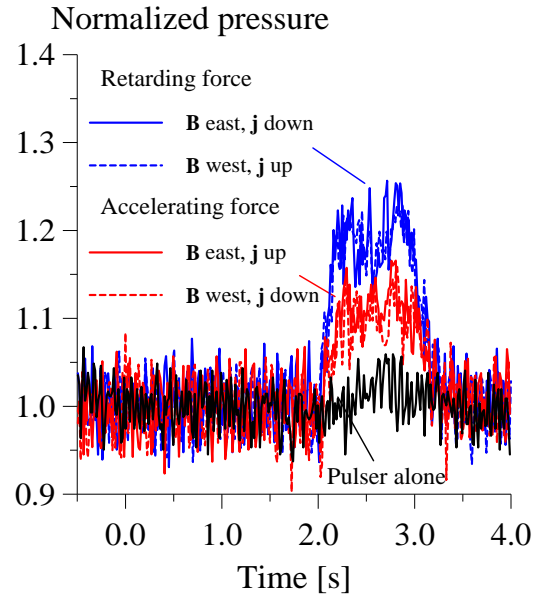


Figure 13. Normalized static pressure traces in a M=4 nitrogen flow at $P_0=600$ torr, $P_{\text{test}}=4.8$ torr, $B=1.63$ T, $\nu=100$ kHz. $U_{\text{PS}}=1.4$ kV, and $R=0.5$ k Ω . Lorentz force is applied for 1 sec duration.

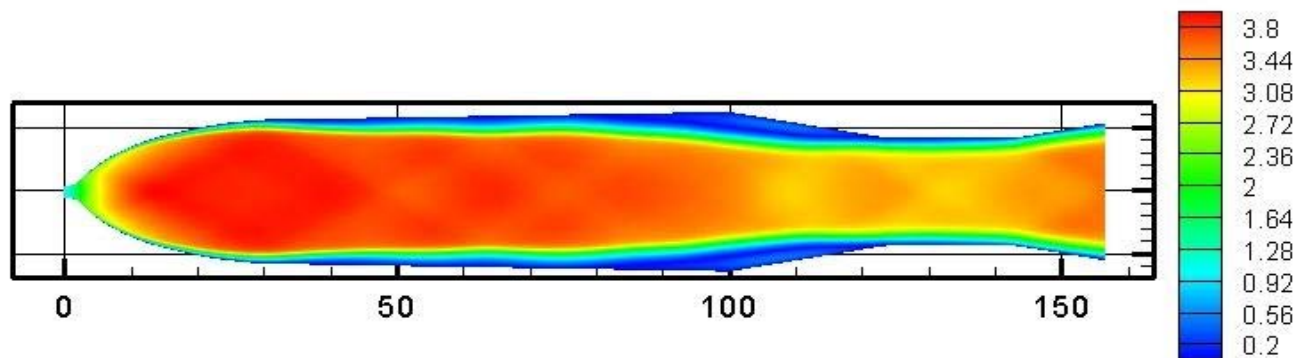


Figure 14. Mach number distribution in a baseline $M=4$ nitrogen flow.

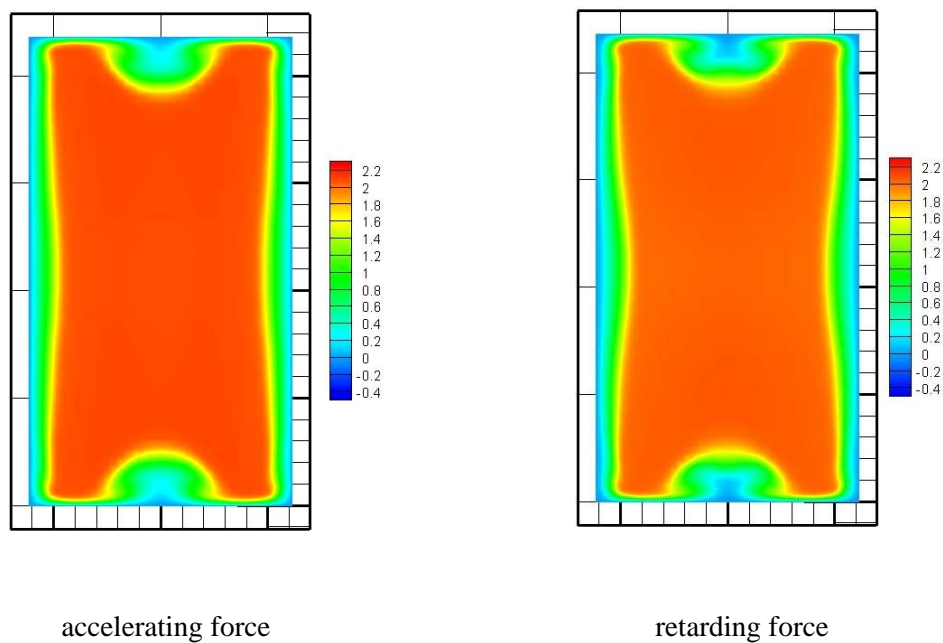


Figure 15. Normalized axial velocity distributions at the end of the MHD section for the accelerated and retarding Lorentz force directions.

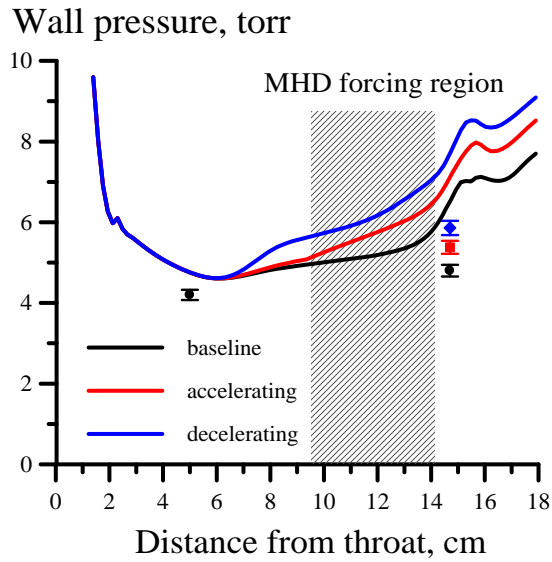


Figure 16. Static pressure distributions along the side (contoured) wall for the baseline, accelerated, and retarded M=4 nitrogen flows. Location of the pulser-sustainer discharge is shown.

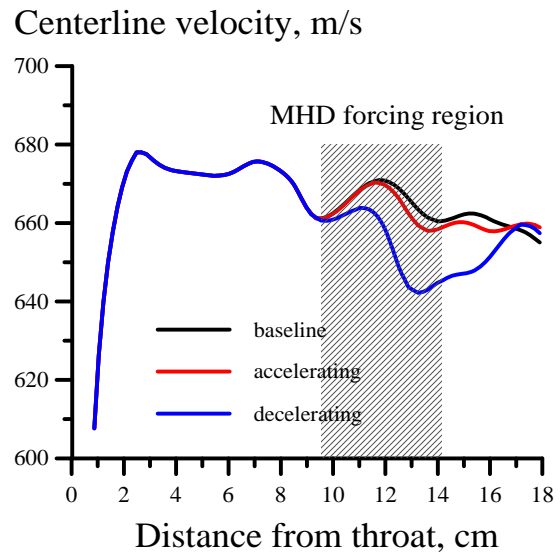


Figure 17. Centerline axial velocity distributions for the baseline, accelerated, and retarded M=4 nitrogen flows. Location of the pulser-sustainer discharge is shown.